Journal of Drug Delivery Science and Technology 123 (2026) 108520

Contents lists available at ScienceDirect

Journal of Drug Delivery Science and Technology

journal homepage: www.elsevier.com/locate/jddst

Preparation and characterization of nano-isoliquiritigenin, molecular dynamics simulations and in vitro studies to evaluate potential TrkB activation

Sara Manin [a,b,c], Edoardo Donadoni [d], Sara Merlo [b], Angela Bonaccorso [b,c], Sonya Salamone [b,c,f], Giulia Frigerio [d], Paulo Siani [d], Josè Maria Lo Faro [g,h], Teresa Musumeci [b,c,*], Cristiana Di Valentin [d,e], Rosario Pignatello [b,c]

[a] PhD in Basic and Applied Biomedical Sciences, Department of Biomedical and Biotechnological Sciences University of Catania, Via Santa Sofia 97, Catania, 95123, Italy
[b] Department of Drug and Health Sciences University of Catania, Via Valdisavoia, 5., Catania, 95123, Italy
[c] Research Centre for Nanomedicine (Nanomed), Department of Drug and Health Sciences University of Catania, Italy
[d] Department of Materials Science, University of Milan-Bicocca, Milan, 20125, Italy
[e] BioNanoMedicine Center, (NANOMIB), University of Milan-Bicocca, Vedano al Lambro, Milan, 20854, Italy
[f] PhD in Neuroscience, Department of Biomedical and Biotechnological Sciences University of Catania, Via Santa Sofia 97, Catania, 95123, Italy
[g] Department of Physics and Astronomy, University of Catania, Via Santa Sofia 64, Catania, 95123, Italy
[h] CNR-IMM, Via Santa Sofia 64, Catania, 95123, Italy

ARTICLE INFO

Keywords:
Isoliquiritigenin
Nanonization
TrkB
Molecular dynamics
SH-SY5Y cells
DoE

ABSTRACT

Natural bioactive compounds are increasingly recognized for their therapeutic potential. Among them, isoliquiritigenin is known for its promising pharmacological potential such as anti-inflammatory, antioxidant, antiobesity, neuroprotective and antitumoral properties. However, its clinical translation is often limited by poor solubility, and consequently, low bioavailability. To overcome these limitations, after the construction of the space of knowledge, using the Design of Experiments approach, we designed and optimized a nano-isoliquiritigenin formulation, produced by nanonization technology. We identified the concentration (0.5 %w/v) and the type (PVP) of stabilizer (independent variables) to obtain a stable formulation with uniform and monodisperse particle size (mean size<100 nm and PDI< 0.2). The interaction between isoliquiritigenin and TrkB receptor was investigated through the molecular dynamic simulations using 7,8-dihydroxyflavone, a well-known TrkB agonist, as a positive control. These preliminary computational findings were validated in SH-SY5Y neuronal-like cells, where isoliquiritigenin and nano-isoliquiritigenin significantly attenuated rotenone-induced toxicity, an effect abrogated by the selective TrkB antagonist ANA-12.

Overall, these results revealed that Design of experiment approach, in particular D-optimal design, is a useful and reliable approach to design and optimized an innovative formulation of nano-isoliquiritigenin obtained by sonoprecipitation technique. In addition, computational and in vitro studies showed promising evidence about the isoliquiritigenin activity as TrkB agonist in neuroprotection, supporting their potential as a novel class of small-molecule TrKB agonist.

1. Introduction

Natural bioactive compounds constitute a promising strategy to clinical applications, thanks to their safety profile and multi-target potential [1]. Among the wide range of natural bioactive molecules, isoliquiritigenin (ILQ), a flavonoid derived from liquorice root (Glycyrrhiza spp.), exhibiting promising pharmacological properties, including anti-tumor, anti-inflammatory, antioxidant, antiobesity and neuroprotective effects [2–7]. However, ILQ clinical application is hampered by its poor water solubility, and limited bioavailability. These challenges can be addressed by employing nanonization technique, that by reducing the particle size of drugs to the nanoscale, offers promising solutions to these

* Corresponding author. Department of Drug and Health Sciences, University of Catania, Via Valdisavoia, 5. 95123, Catania, Italy.
E-mail address: teresa.musumeci@unict.it (T. Musumeci).

https://doi.org/10.1016/j.jddst.2026.108520
Received 19 November 2025; Received in revised form 16 April 2026; Accepted 25 May 2026
Available online 26 May 2026

limitations [8–12]. Nanonization process allows us to obtain submicron colloidal dispersions of nanosized drug particles and one or more stabilizers, (surfactants and or polymers, or a mixture of both) [13]. Nano-drug are carrier-free particles characterized by high drug concentrations, leading to enhanced pharmacokinetic properties compared to the free-drug [14,15]. Formulations obtained by nanonization process are easy to produce on a large scale at low cost. They are mainly applied to oral drug delivery, and other drug delivery routes, such as, injection, ocular and nose to brain delivery [10,16–18].

Recent studies have highlighted that ILQ administration in rat model of cognitive impairment can increase brain derived neurotrophic factor (BDNF) levels, however the mechanism involved in this process needs further investigations [7,19]. BDNF possesses a poor pharmacokinetic profile that limits its clinical application: its high molecular weight impedes the passage through the blood brain barrier (BBB) and its plasma half-life in rats is less than 1 min. Different efforts were made to synthetize small molecules capable of activating the tyrosine kinase B (TrkB) receptor with high selectively and specificity [20]. In 2010, the natural derived product 7,8-dihydroxyflavone (7,8-DHF) was identified by Jang et al. as a selective TrkB receptor agonist mimicking BDNF actions [21,22]. TrkB receptor is a member of the neurotrophin receptor tyrosine kinase family which mediates the main biological action of BDNF. The binding between BDNF and TrkB induces the activation of three main signaling cascades: the Ras/Raf/MEK/mitogen-activated protein kinase pathway, phosphatidylinositol 3-kinase, and phospholipase C-γ, producing effects on neuronal growth, survival and synaptic plasticity [23].

In this context, the aim of this work is to explore the BDNF/TrkB neurotrophic activity of ILQ and assess its potential as a TrkB agonist, increasing its intrinsic low solubility. For this purpose, nano-ILQ was designed, developed and optimized through Design of Experiment (DoE) in combination with a solvent–antisolvent sonoprecipitation method to amplify the dissolution rate of the molecule. In the experimental domain, the stabilizer type and its concentration (independent variables) have been chosen respectively as categoric factor and numeric factors, while mean size (nm), polydispersity index and Zeta Potential as output (responses).

The optimized nano-ILQ was further characterized in pH, osmolarity and morphology. Stability studies of nano-ILQ at different storage conditions (4 °C, 25 °C, 37 °C) were carried out for six months.

Furthermore, the potential agonist activity of ILQ at the TrkB receptor, was explored through computational studies based on molecular docking and steered molecular dynamics/umbrella sampling, followed by in vitro verification of TrkB receptor-mediated neuroprotection using neuronal-like SHSY-5Y cells. The TrkB receptor agonist 7,8-DHF was used as a positive control. In anticipation of in vitro studies, stability of 7,8-DHF and ILQ was monitored at 37 °C for one week.

2. Materials and methods

ILQ was purchased from MedChemExpress (MCE). 7,8-DHF, Ethanol, polyvinylalcohol (PVA), polyvinylpyrrolidone (PVP) and dimethyl sulfoxide (DMSO), the selective TrkB receptor antagonist ANA-12, rotenone and 3-[4,5-dimethylthiazol-2-yl]-2,5-diphenyltetrazoliumbromide (MTT) were provided by Sigma-Aldrich (Merck Life Science S.r.l., Milan, Italy). Kolliphor P188 (P188) was obtained from BASF (Ludwigshafen, Germany).

The human neuroblastoma SH-SY5Y cell line was purchased from ATCC (Manassas, VA, USA; catalog # CRL-226). Cells were grown in DMEM/F12 supplemented with 10% fetal bovine serum (FBS) and penicillin (100 U/ml)/streptomycin (100 μg/ml) solution (all from Thermofisher Scientific, Milan, Italy) and were maintained at 37 °C in a CO_2 incubator (Thermofisher).

2.1. Design of experiment

2.1.1. Construction of experimental space

To delineate the space of knowledge, we collected scientific articles published from 2018 to 2023, concerning the preparation and characterization of nanocrystals. Among the available literature, only the study by Yanni Ma et al. (2022) was found to be consistent with the keywords “isoliquiritigenin nanocrystals” and “nanoisoliquiritigenin”. Futhermore, in view of a potential future intranasal application of the formulation, we included the keywords “intranasal nanocrystal” and “nose-to-brain nanocrystal” to identify stabilizers suitable for this route of administration.

The space of knowledge allowed us to identify all the critical material attributes (CMAs) that could be involved in the quality target profile of the optimized formulation of our interest. Based on the space of knowledge, the CMAs were chosen, and the experimental design was built.

The experimental design of nano-ILQ formulations was obtained using Design-Expert software (Design Expert software version 13 - StatEase®). One numeric factor corresponding to the amount of stabilizer expressed as %W/V stabilizer/aqueous phase, was selected at three levels: 0.5-1-1.5%W/V. These three levels allowed us to consider the lowest concentration of our numeric factor, the highest concentration and one intermediate value of this.

A categoric factor was also selected in the design of the experiments, corresponding to the nature of stabilizers, and those selected were P188, PVA and PVP.

The model used to build the design is the Optimal Custom Design, specifically D-optimal, which produces a design that best estimates the effects of the factors, it is particularly suited for screening studies. A total of ten runs were carried out to evaluate the effect of the independent variables on Mean Size (nm) and Zeta Potential (mV) responses (Table 1).

For the statistical computations, the independent variables, stabilizer concentration and stabilizer type, were denoted as X_1 and X_2, respectively. Statistical analysis of data was performed by ANOVA, provided in the software.

2.1.2. Sonoprecipitation technique to obtain nano-isoliquiritigenin

Nano-ILQ were prepared by the sonoprecipitation method which combines precipitation and ultrasonication using a probe sonicator (Branson sonifier 450, Marshall Scientific, Hampton, NY, USA). The solvent phase was composed of 5 mg of ILQ powder solubilized in 250 μl of ethanol. The antisolvent phase was prepared by dissolving different concentrations (0.5, 1, 1.5% W/V) and types (P188, PVP, PVA) of stabilizers according to the experimental design. After complete dissolution of ILQ, the solvent phase was dropped into 2.5 ml of antisolvent phase, under magnetic stirring (500 rpm), followed by intense sonication using a probe immersed 6 mm in the liquid. Sonication was carried out at a power input of 400 W for 10 min using a continuous cycle. The ultrasonic sound burst was maintained at a constant frequency, and the

Table 1
Runs obtained from D-Optimal design.

RUNS	Stabilizer (%W/V)	Stabilizer type	Mean Size (nm)	Zeta Potential (mV)
1	1	PVP	257.7	−28.9
2	0.5	PVP	87.97	−40.3
3	0.5	PVA	866.5	−17.3
4	1.5	PVA	1035	−11
5	0.5	P188	759.3	−32.9
6	0.5	PVP	86.59	−40
7	1.5	P188	622.4	−32
8	1	P188	844.7	−29.7
9	1	PVA	733.3	−14.2
10	1.5	PVP	391.1	−25.9

temperature, during the sonication process, was stabilized using an ice-water bath. To evaporate the ethanol, the formulations were kept under a fume hood and under magnetic agitation for 15 min. Then, the spontaneous formation of nano-ILQ was confirmed by the appearance of a slightly turbid suspension.

2.1.3. Mean size, polydispersity and zeta potential analysis

Photon Correlation Spectroscopy (PCS; Zetasizer Nano S90; Malvern Instruments, Malvern, UK) was employed to determine the particle mean size (nm), Polydispersity Index (PDI), and Zeta Potential (mV) of nano-ILQ at a detection angle of 90 °C, at 25 °C with a 4 mW He – Ne laser operating at 633 nm. All measurements were performed for nano-ILQ after dilution 1:10 using water. The measurements were conducted in triplicate, and the obtained results are reported as mean ± Standard Deviation (SD).

2.1.4. Nano-isoliquiritigenin optimization

Nano-ILQ optimization was performed using the 'desirability tool' provided by the Design of Experiment software. The software independently combines all levels of the independent variables considered (X_1 and X_2) in order to identify the optimal condition within the experimental domain. The results obtained are expressed as 'desirability', which is a function whose values range from 0 to 1, where 1 corresponds to the desired value.

2.2. Physico-chemical characterization of optimized formulation

2.2.1. Morphology observation

The morphology of nano-ILQ was determined using a Scanning Electron Microscope (SEM) by using a GEMINI field effect microscope from ZEISS. To acquire the SEM analyses, a sample of nano-ILQ (dilution 1:10) was obtained by spin coating the solution onto a Si wafer piece at 500 rpm for 1 min with a WS-400 instrument from Laurell Technologies and left to dry in air.

2.2.2. Storage stability study of nano-ILQ

The samples were stored at the accelerated condition (40 ± 2 °C/ 75% RH ± 5% RH) according to ICH guidelines, at room temperature (25 ± 2 °C), and at 4 ± 2 °C in order to evaluate the stability of nano-ILQ from time zero (T0) to six months. Stability measurements were performed at predetermined times (T0, 7 days, 15 days, from 1 month to 6 months), to assess changes in mean size (nm), PDI and Zeta Potential (mV). All studies were conducted in triplicate.

2.2.3. pH and osmolarity evaluations

The nano-ILQ pH was determined at 25 ± 2 °C by using a pH-meter (Mettler Toledo, Columbus, OH, USA). The instrument was calibrated by using buffer solutions (pH 4.01 ± 0.02; 7.00 ± 0.02 and 10.00 ± 0.02; slope 99.8%; Mettler Toledo, Columbus, OH, USA). Measurements were performed in triplicate and results were expressed as the mean ± SD. The nano-ILQ osmolarity was determined using a freezing point osmometer (Osmomat 3000, Gonotec). Deionized water (0 mOsmo/kg) and two calibration standards (300 mOsmol/kg and 850 mOsmol/kg) were used for three points calibration. Samples were measured in triplicate and results were expressed as the mean ± SD.

2.3. Computational studies

2.3.1. Docking calculations

System preparation and molecular docking calculations were performed using the Glide module within the Schrödinger Suite (release 2021-1) ("Schrödinger Release 2021-1: Maestro, Schrödinger, LLC, New York, NY, 2021."). The X-ray crystal structure of the TrkB-d5 domain (hereafter referred to as TrkB; PDB ID: 1HCF, 2.7 Å resolution) [24] was prepared using the Protein Preparation Wizard [25], during which hydrogen atoms were added and protonation states of titratable amino acid residues were assigned for pH 7.0, based on their predicted pK_a values. The ligands, 7,8-DHF and ILQ, were prepared using LigPrep ("Schrödinger Release 2021-1: LigPrep, Schrödinger, LLC, New York, NY, 2021."), with proper tautomeric and ionization states generated for pH 7.0. Induced Fit Docking was carried out using Glide [26] in combination with the OPLS_2005 force field [27]. Docking poses were evaluated and ranked using the Glide Extra Precision (XP) scoring function to ensure reliable identification of the most favorable binding configurations.

2.3.2. Molecular dynamics simulations and free energy calculations

The protein–ligand complexes were prepared for molecular dynamics (MD) simulations with the CHARMM-GUI web server [28], which assigned CHARMM36 [29] and CGenFF [30–32] parameters to the protein and the ligand, respectively. The complexes were embedded in parallelepiped-shaped simulation boxes (dimensions: 140 × 80 × 80 $Å^3$) filled with mTIP3P water molecules [33], using GROMACS preparation tools [34]. Sodium (Na^+) and chloride (Cl^-) ions [35,36] were added to neutralize the system and reproduce a physiological ionic strength of 0.15 M. The initial structures were those obtained from docking calculations.

All systems underwent energy minimization using the steepest descent algorithm. The free energy calculation protocol comprised two sequential steps: Steered Molecular Dynamics (SMD) followed by Umbrella Sampling (US). In the SMD step, a predefined reaction coordinate (ξ), corresponding to the unbinding pathway of the ligand from the protein, was sampled. The ligand and surrounding TrkB residues (within 5 Å of the ligand, as identified in the docking pose) were gradually separated by applying a harmonic biasing potential between their centers of mass (COMs). Pulling was performed along the x-axis using a force constant of 1000 kJ mol^{-1} nm^{-2} and a pulling rate of 0.01 nm ps^{-1}. Configurations were extracted every 0.1 nm along the COM distance and used as initial structures for subsequent US.

Each US window was simulated for 12 ns under NPT conditions (310 K, 1 atm), with the first 2 ns treated as equilibration and the remaining 10 ns used for analysis. A harmonic restraint of 1000 kJ mol^{-1} nm^{-2} was applied to maintain the target COM separation. Temperature and pressure were regulated using the V-rescale thermostat [37] (coupling constant of 1.0 ps) and the Parrinello–Rahman barostat [38] (coupling constant of 2.0 ps), respectively. Bond lengths involving hydrogen atoms were constrained using the LINCS algorithm [39], and the Velocity-Verlet leap-frog integrator was employed with a 2.0 fs timestep. Long-range electrostatic interactions were computed using the Particle Mesh Ewald (PME) method [40] with a 12 Å cutoff, while van der Waals interactions were calculated via the Lennard-Jones potential with the same cutoff. Lorentz–Berthelot combining rules were applied, and Periodic Boundary Conditions (PBC) were imposed in all directions.

All SMD and US simulations were carried out using the GROMACS simulation package [34]. The Potential of Mean Force (PMF) was reconstructed from the US data using the Weighted Histogram Analysis Method (WHAM) [41], as implemented in GROMACS. WHAM calculations utilized 300 bins per nm and 100 bootstrap iterations to generate average PMF profiles and associated statistical uncertainties. To enhance statistical robustness, umbrella histograms were weighted according to their integrated autocorrelation times (IACTs), smoothed along ξ using Gaussian kernels with a standard deviation of σ = 0.15 nm [42].

From the PMF profiles, we extracted the binding free energy, $\Delta G_{binding}$, defined as the Gibbs free energy difference between the bound and unbound states of the protein–ligand complex (Equation (1)).

$$\Delta G_{binding} = G_{bound} - G_{unbound} \quad (1)$$

2.4. In vitro assays on SHSY-5Y cell lines

2.4.1. UV-vis measurements to assess stability of molecules at 37 °C

Prior to in vitro studies, the in-solution stability of ILQ and 7,8-DHF was tested by UV–Vis spectroscopy (UH5300 UV–Visible Double-Beam Spectrophotometer, Hitachi Europe, Milan, Italy). Stability studies of ILQ and 7,8-DHF, were carried out in DMSO. The molecules were weighed and solubilized in the solvent (20 μg/mL) to study their different behaviour.

After the dissolution of samples, they were stored in capped ambered vials separately in the incubator (37 °C), and withdrawn at precise time intervals (T0, 1, 2, 3, 6, 24, 72, 168 h) to assess thermal stability. The content of drug was measured by UV-Vis spectra that were collected at room temperature using a quartz cuvette with 1 cm path length and the following parameters: 250–400 nm wavelength range, 200 nm/min scanning speed. The optimum absorption wavelengths were 270 nm for 7,8-DHF and 380 nm for ILQ. The studies were conducted in triplicate to perform a statistical analysis. The storage stability was calculated basing on the following Equation (2):

$$\text{Percentage of drug degradation } (\%) = \frac{\text{retained absorbance}}{\text{initial absorbance}} \text{ x } 100 \quad (2)$$

2.4.2. MTT cell viability assay

SH-SY5Y cells were plated at a density of $50{\cdot}10^3$ cells/well in a 96-well microplate (Corning) on the day before the experiment and serum-deprived at the time of treatment. The TrkB receptor antagonist ANA12 (10 μM) was always added 30 min before the tested drugs. ILQ, nano-ILQ or 7,8-DHF (all at a final concentration of 10 μM) were added 30 min prior to challenge with rotenone (150 nM for 24 h). The MTT substrate (0.5 mg/mL) was added during the last 1.5 h of treatment; medium was then removed, and cells were incubated with DMSO for 10 min at 37 °C to solubilize formazan crystals. Readings were carried out at 545 nm using a Varioskan™ Flash Multimode Reader (Thermofisher). Statistical analysis was carried out by one-way ANOVA followed by Uncorrected Fisher's LSD multiple comparison test for significance, using the Graphpad Prism 9.0 software. Data were from at least 3 experiments run at least in triplicate.

3. Results and discussion

3.1. Experimental design

The design of experiment approach, combining all selected factors to evaluate their impact in the critical quality attributes of the formulations, allowed us to obtain the highest information by reducing the number of experiments. By identifying and selecting independent variables and responses the experimental space was built.

The pre-optimization studies concluded that both the type of stabilizer and its concentration significantly influenced the mean size and Zeta potential. The formulations showed a mean size ranging from 87.86 ± 0.8 nm to 1035 ± 53.8 nm reflecting the influence of independent variables on nano-ILQ size (Fig. 1). PDI values remained below 0.3, that is generally the limit accepted for qualitative formulations, suggesting uniform size distributions. However, some runs exhibited higher variability (e.g., run 9 and run 4) (Fig. 1) [43]. Since PDI did not show statistical significance within the constructed model, it was excluded from the set of response variables used for the model optimization. In Fig. 1, the results of Zeta potential (mV) are reported, all formulations exhibit negative surface charges, with a maximum Zeta potential value at −40.3 ± 0.6 mV.

ANOVA was used to analyze the impact of independent variables, X_1 and X_2, on the dependent variables, means size (Y_1) and Zeta potential (Y_2). Fig. 2 (panel A) illustrates the effect of X_1 and X_2 on Y_1. PVP (red line) produces the smallest nano-ILQ size (87.86 ± 0.8 nm), instead PVA (green line) and P188 (blue line) produce significantly larger nano-ILQ. Moreover, increasing stabilizer concentration resulted in a more pronounced increase in mean size. This indicates that both stabilizer type and amount critically influence means size. Panel B of Fig. 2 illustrates the effect of X_1 and X_2 on Y_2. PVP (red line) exhibits the most negative Zeta Potential values (−40.3 ± 0.5 mV), implying better electrostatic stabilization, in contrast with PVA (green line) and P188 (blue line). Furthermore, by decreasing the concentration of stabilizers, the zeta potential takes a more negative value, indicating greater stability of the formulations.

3.1.1. Effect of independent variables on mean size (Y1)

Using the statical linear model, a polynomial regression analysis was performed on the response Y_1 to determine the coefficients of the model terms. In the polynomial equation (3) provided by the software, the concentration of stabilizer (%W/V) corresponds to the term A and type of stabilizer corresponds to term B. In addition, positive coefficient indicates that as the value of the independent variable increases, the dependent variable also tends to increase. On the contrary, a negative coefficient suggests that as the independent variable increases, the dependent variable tends to decrease.

This equation expresses the predicted response of nano-ILQ mean size in terms of actual factors:

$$Y_1 = 222.65 + 67.26 * A + 655.61 * B[1] + 519.48 * B[2] \quad (3)$$

In this case term B was found to be statistically significant. The positive coefficient associated with B [1] (+655.61), indicates that PVA produces significantly larger nano-ILQ than PVP. Similarly, the coefficient of B [2] (+519.48), which refers to P188, shows a significant increase compared to PVP, although slightly smaller than those obtained with PVA. Our results suggest that PVP appears to be the most effective

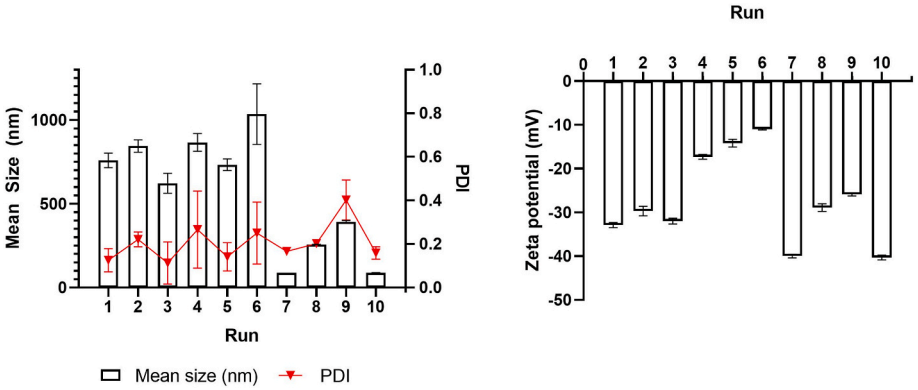

Fig. 1. Mean size (nm), Polydispersity Index (PDI) and Zeta Potential (mV) obtained following the production of the nanoformulations obtained by experimental space.

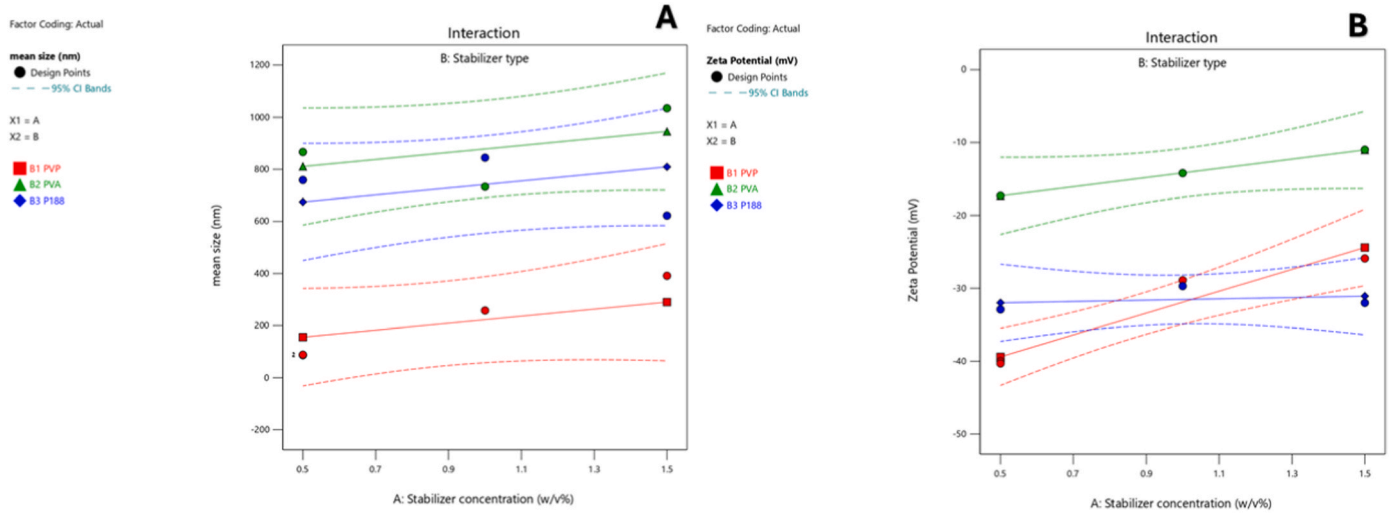

Fig. 2. Influence of independent variables (stabilizer type and stabilizer concentration) on mean size (nm) (A), and Zeta potential (mV) (B).

at yielding smaller nano-ILQ among the three stabilizers, as both PVA and P188 add a positive increment to the baseline size when compared to PVP. PVA results in the largest nano-ILQ, followed by P188 (519.48 units larger than PVP). Furthermore, ANOVA analysis demonstrates that the model is statistically significant, with an F-value of 17.73 and a corresponding p-value of 0.0022, indicating that the factors included explain a meaningful portion of the variability. The R^2 of 0.8986 indicates that approximately 89.86% of the variation in the response can be explained by the model, which reflects a strong correlation between the obtained values and the predicted values. The Adequate Precision value of 9.4231, which measures the signal-to-noise ratio, is over the desirable threshold of 4. This confirms that the model has an adequate signal and can be used to navigate the design space. Among the stabilizers used for preparation of nano-ILQ, PVP has consistently shown better performance compared to PVA and P188. This is probably due to the capacity of PVP to form stabilizing interactions, hydrogen bonding and van der Waals forces, with the surface of drug particles. These interactions promote a more efficient adsorption of the stabilizer onto the nano-ILQ surface, resulting in improved dispersion and reduced aggregation. Moreover, the molecular structure of PVP allows it to create a thin steric barrier around nano-ILQ, enhancing physical stability [12,44,45]. PVA, while helpful in reducing particle size due to its emulsifying properties, often leaves behind residual layers and does not provide the same level of steric hindrance [12]. P188, a block copolymer, tends to offer weaker surface coverage due to its bulkier structure, which may lead to larger and less stable particles over time [46,47].

3.1.2. *Effect of independent variables on nano-ILQ zeta potential (Y_2)*

A polynomial regression analysis was performed on response Y_2 to determine the coefficients of the model terms. Even then, the predicted response of nano-ILQ Zeta potential is expressed by the polynomial equation (4), provided by the software.

$$Y_2 = -31.90 + 7.50 * A + 17.73 * B\,[1] + 0.3667 * B\,[2] - 4.35 * AB\,[1] - 7.05 * AB\,[2] \quad (4)$$

The equation shows the quantitative effect exerted by the independent variables on Zeta Potential response (Y_2) and in this case, both A and B were significant model terms. The term A represents the linear effect of stabilizer concentration when using PVP. For every one unit increase in stabilizer concentration, the zeta potential is expected to increase by 7.50 units (mV) when PVP is the stabilizer. The term B (stabilizer type) was found significant with B[1], and B[2] positive coefficients, +17.73 and + 0.3667 respectively suggesting that, the zeta potential is predicted to be higher than with PVP and that this effect is much smaller with P188 compared with PVA. These findings indicate that PVP provides the most significant change in zeta potential with increasing concentration, showing a strong positive slope. PVA also increases zeta potential with concentration, but at a significantly reduced rate compared to PVP, while P188 shows very little change in zeta potential with increasing concentration, almost flat-lining.

Furthermore, ANOVA analysis demonstrates that the model (2FI) is statistically significant, with an F-value of 41.86 and a corresponding p-value of 0.0015. This low p-value indicates that the model terms have a significant effect on the response variable, and the probability that this outcome is due to random chance is only 0.15%. The R^2 value is 0.9812 indicating that 98.12% of the variability in the response is explained by the model, it suggests that the model predictions are closely aligned with the actual data and that it captures nearly all the relevant trends in the dataset. The high Adequate Precision value of 17.5370 confirms the robustness of the model. These results confirm that the model can be used to navigate the design space and make meaningful predictions. Among the stabilizers tested, PVP demonstrated a stronger effect on surface charge compared to PVA, as indicated by the highly significant p-value for Factor B ($p = 0.0006$). This observation aligns with previous studies showing that PVP enhances surface stabilization contributing to more negative and stable Zeta potential [48]. The stabilizer concentration was also significant ($p = 0.0069$), confirming that the amount of stabilizer modulates surface charge density, likely by influencing the coverage and thickness of the stabilizing layer. Notably, the interaction between concentration and stabilizer type (AB) was marginally significant ($p = 0.0505$), suggesting that the effect of concentration on Zeta potential depends on the stabilizer used. This supports the hypothesis that PVP and PVA respond differently to increasing concentrations, potentially due to differences in their molecular conformation and surface adsorption behavior.

3.2. *Optimization process*

Statistical data showed that the concentration of PVP exerted a significant impact on the mean size of nano-ILQ. Based on ANOVA analysis, the factors and the desired responses were set in order to obtain an optimized formulation of nano-ILQ. Factors and desired response are listed in Table 2.

We aimed to minimize mean size and Zeta potential in order to obtain optimized nano-ILQ. Setting these parameters, the software provided one optimized formulation with a desirability value of 0.965, selecting PVP as stabilizer type at the concentration of 0.5 %W/V. To test the predictivity, the optimized formulation was prepared in

Table 2
Parameters to optimize nano-ILQ.

Factors and Response	GOAL
Stabilizer concentration	minimize
Stabilizer type	PVP
Mean Size (nm)	minimize
Zeta Potential	minimize

triplicate, and it was characterized by PCS analysis.

PCS analysis, particularly size distribution by intensity, revealed a monodisperse system with a mean size population of 81.87 ± 0.5 nm with a PDI of 0.16 ± 0.01 (Figs. S3 and S4) suggesting a uniform population of nano-ILQ and the absence of significant aggregation and larger secondary populations, in fact no secondary peaks were observed. The correlograms showed a sharp and smooth decay of the correlation coefficient, which correlates with a monodisperse suspension with uniform Brownian motion, a homogeneous particle population with no aggregates or polydispersed subpopulations (Fig. S3). The optimized formulation shows a negative zeta potential −38.36 ± 0.46 mV (Fig. S4), this value suggests excellent colloidal stability due to electrostatic repulsion between particles, in fact zeta potential values more negative than −30 mV or more positive than +30 mV are generally regarded as stable. Data obtained by PCS characterization revealed that an optimized formulation of nano-ILQ was obtained, combining the DoE approach and the sonoprecipitation method. In addition, the use of PVP as stabilizing agent was essential to obtain a stable and monodisperse nanosuspension.

3.2.1. Morphological, physico-chemical characterization and storage stability of optimized nano-ILQ

The SEM image (Fig. 3 A) reveals that the nano-ILQ are predominantly spherical in shape and exhibit a relatively uniform size distribution across the substrate. The nano-ILQ display smooth surfaces with minimal agglomeration, suggesting effective dispersion and stabilization during preparation. The diameters of the nano-ILQ range approximately from 30 to 80 nm, although some larger aggregates are observed due to the dried process performed for specific analyses.

The histogram in Fig. 3 B presents the frequency distribution of nano-ILQ sizes based on various dimensional descriptors: ellipsoidal major (black bars) and minor (red bars) axes, maximum (blue bars) and minimum (cyan bars) Feret's diameters. The data was obtained via pixel-based particle size analysis using *ImageJ*, where individual nano-ILQ dimensions were extracted from SEM micrographs and categorized accordingly by fitting the pixel with an ellipse, or considering the external and internal circle enveloping the particle. Gaussian fits were applied to each dataset to determine mean value and distribution characteristics are shown in Fig. 3 B for each parameter: solid black and red lines for the ellipsoidal major and minor axes respectively, solid blue and cyan lined for the maximum and minimum Feret's diameters. The average value for the mean diameters obtained from the Gauss fit is reported for each parameter in the following Table 3.

The mean diameter for the nano-ILQ obtained averaging the ellipsoidal major and minor axis is about 42 ± 3 nm, and of about 46 ± 3 nm in the case of maximum and minimum Feret' diameters.

These results demonstrate a small variation between the ellipsoidal major and minor axes, as for the maximum and minimum Feret diameters, suggesting that the nano-ILQ are nearly spherical or only slightly ellipsoidal in shape. An ellipse with an eccentricity of 0.6 is moderately elongated, lying between a perfect circle (with eccentricity equal to 0) and a very stretched ellipse approaching a parabola (with eccentricity close to the value of 1). This level of eccentricity indicates that the nano-ILQ **has** a noticeable but not extreme elongation, consistent with shapes that are oval-like or elliptical, rather than circular. The relatively small difference (within ~10–15 nm) between these values indicates a low degree of anisotropy.

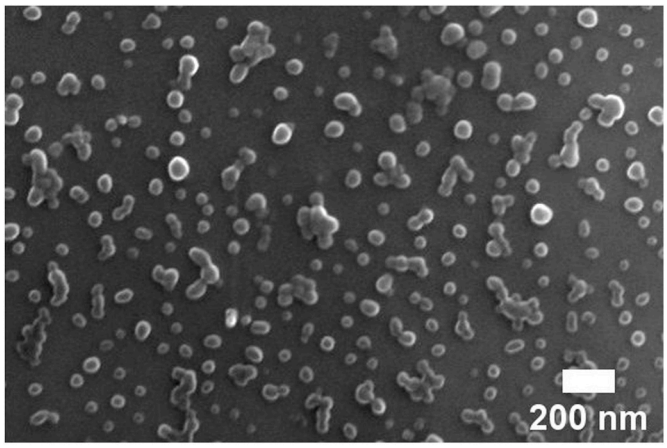

A

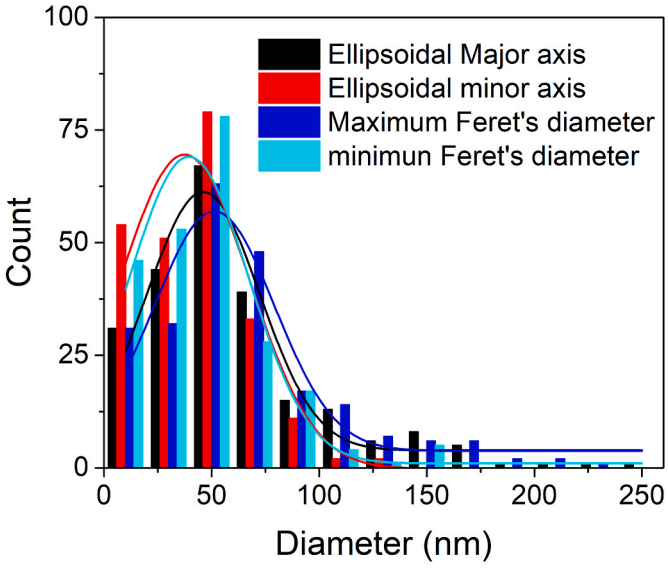

B

Fig. 3. A) Plan-view Scanning Electron Microscopy (SEM) image showing the morphology of nano-ILQ. A 100 μL aliquot of a 1:10 dilution from a 2 mg/mL nano-ILQ solution was spin-coated onto a silicon substrate prior to imaging. B) Frequency count histogram for ellipsoidal major (black bars) and minor (red bars) axes, maximum (blue bars) and minimum (cyan bars) Feret's diameters. The solid lines correspond to the Gauss fits of each parameter: solid black and red lines for the ellipsoidal major and minor axes respectively, solid blue and cyan lined for the maximum and minimum Feret's diameters. (For interpretation of the references to color in this figure legend, the reader is referred to the Web version of this article.)

Additionally, the narrow width of the Gaussian distributions and the high R^2 values (all >0.89) confirm that the nanoparticle population exhibits a high degree of size uniformity and consistent morphology.

It is worth noting that these size values, obtained from SEM, are generally smaller than those measured by Dynamic Light Scattering (DLS), which reflects the hydrodynamic diameter of the particles in suspension. This discrepancy is expected, as DLS captures the particle size including any solvation shell and associated surface molecules, whereas SEM measures the dry, core physical size of the nano-ILQ.

The long-term stability studies were performed with the aim of

Table 3
Shape descriptor.

Ellipsoidal Major axis (nm)	Ellipsoidal minor axis (nm)	Ratio EMajor/ Eminor	Eccentricity	Maximum Feret Diameter (nm)	Minimum Feret Diameter (nm)	Feret Ratio
46 ± 2	38 ± 4	1.2 ± 0.1	0.6 ± 0.1	51 ± 2	40 ± 3	1.3 ± 0.1

assessing the long storage stability of nano-ILQ at 40 °C, 25 °C and 4 °C up to 6 months in terms of mean size, PDI and Zeta potential by PCS analysis. Results showed that nano-ILQ were unstable after one week of storage at both 40 °C and 25 °C (data not reported).

The data collected from stability studies at 4 °C are reported in Fig. 4. The results show a mean size almost unchanged over time, remaining within a narrow range, suggesting good colloidal stability (Fig. 4 panel A). PDI value remained almost unchanged for all formulations, it reflects a monodisperse system, with no significant aggregation events observed. Zeta Potential values (Fig. 4 B) did not show difference. In addition, Zeta Potential value is above −40 mV, meaning that nano-ILQ can be considered stable due to the electrical repulsion between the surface charges, reducing the aggregation capacity of systems. The concordance between the dimensional stability and electrokinetic profile supports the robustness of the formulation, indicating its suitability for storage without compromising physicochemical properties.

3.3. Computational results: docking of ILQ (vs 7,8-DHF) to TrkB

As an initial and computationally cheap step, we performed molecular induced-fit docking calculations to identify the most favorable binding poses (i.e., configurations) of 7,8-DHF and ILQ in complex with TrkB-d5 domain, hereafter referred to as TrkB, as detailed in Section 2.3.1.

Fig. 5 and Figs. S1 and S2 present the interaction diagrams of the most stable binding pose of 7,8-DHF (used as a reference molecule) and the eight most stable poses of ILQ ($ILQ^{pose1-8}$), selected according to their GlideScore values (<−6 kcal mol^{-1}, Table 4).

Specifically, 7,8-DHF acts as a hydrogen bond donor to the Thr332 residue (forming two H-bonds) and as a hydrogen bond acceptor from Leu315 (Fig. 5). A very similar interaction pattern was also found by rigid docking calculations performed by Chitranshi et al. [49]. In pose 1, ILQ forms three hydrogen bonds as a donor with Pro313, Leu315, and Gln316, and additionally engages in a cation–π interaction with Lys312 (Fig. S1). In pose 2, ILQ is a hydrogen bond acceptor from Trp317 and donor to Leu324 and Asn325 (Fig. S1). In pose 3, ILQ is a hydrogen bond donor to Leu315 and Glu326, acceptor from Gln316, and forms a cation–π interaction with Lys312 (Fig. S1). In pose 4, ILQ is a hydrogen bond donor to Glu326 and Thr332 and establishes a cation–π interaction with Lys312 (Fig. 5). In pose 5, ILQ is a hydrogen bond donor to Pro313, Leu315, and Leu324 (Fig. 5) – an interaction pattern shared by ILQ^{pose8} (Fig. S2). In pose 6, ILQ is a hydrogen bond donor to Pro313, Leu315, and Gln316 (Fig. S2). Lastly, in pose 7, ILQ interacts with the same residues as in pose 5, but functions as a hydrogen bond acceptor in its interaction with Leu315 (Fig. S2).

Table 4
GlideScore and Δ $G_{binding}$ values from docking and SMD/US calculations for all the investigated protein/ligand configurations.

System	GlideScore (kcal mol^{-1})	Δ $G_{binding}$ (kcal mol^{-1})
TrkB/7,8-DHF	−6.309	−7.1 (±0.6)
TrkB/ILQ^{pose1}	−7.048	−2.1 (±0.5)
TrkB/ILQ^{pose2}	−6.827	−1.4 (±0.5)
TrkB/ILQ^{pose3}	−6.727	−3.3 (±0.3)
TrkB/ILQ^{pose4}	−6.417	−7.4 (±1.9)
TrkB/ILQ^{pose5}	−6.246	−7.5 (±0.7)
TrkB/ILQ^{pose6}	−6.127	−1.2 (±1.5)
TrkB/ILQ^{pose7}	−6.148	−1.0 (±0.2)
TrkB/ILQ^{pose8}	−6.117	−3.0 (±1.7)

With respect to GlideScore values, ILQ exhibits scores that are comparable to, and in some instances more negative than, that of 7,8-DHF, suggesting a similar binding affinity of ILQ and 7,8-DHF for TrkB.

3.3.1. Estimation of binding free energy by umbrella sampling

A more advanced method for deriving thermodynamic data on protein–ligand interactions involves Steered Molecular Dynamics (SMD) and Umbrella Sampling (US) calculations (for further details see Section 2.3.2), which were initiated from the docking-derived poses. In Fig. 5, the potential of mean force (PMF) profiles for 7,8-DHF and the two most favorable ILQ binding configurations with TrkB are superimposed for comparison. Additionally, Table 3 summarizes the estimated Δ $G_{binding}$ values (calculated via Equation (1)) for all examined systems. For completeness, the remaining PMF profiles, not included in Fig. 5, are provided in Figs. S1 and S2 of the Supplementary data.

We note that 7,8-DHF exhibits a Δ $G_{binding}$ of −7.1 (±0.6) kcal mol^{-1}, which is consistent with its GlideScore of −6.309 kcal mol^{-1}. This binding free energy suggests that 7,8-DHF binds effectively to TrkB.

For ILQ, we observe that both ILQ^{pose4} and ILQ^{pose5} exhibit favorable Δ $G_{binding}$ values of −7.4 (±1.9) and −7.5 (±0.7) kcal mol^{-1}, respectively. These values are comparable to, and even slightly more negative

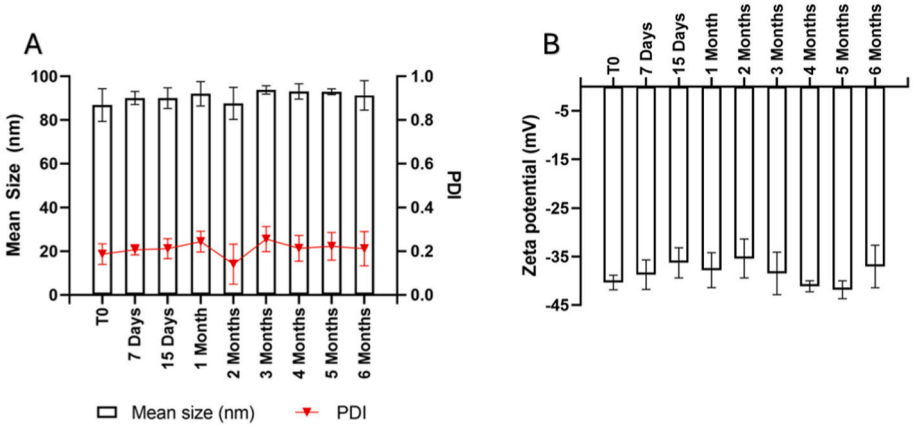

Fig. 4. Stability studies in terms of mean size, PDI (A) and Zeta Potential (B) of nano-ILQ stored at 4 ± 2 °C.

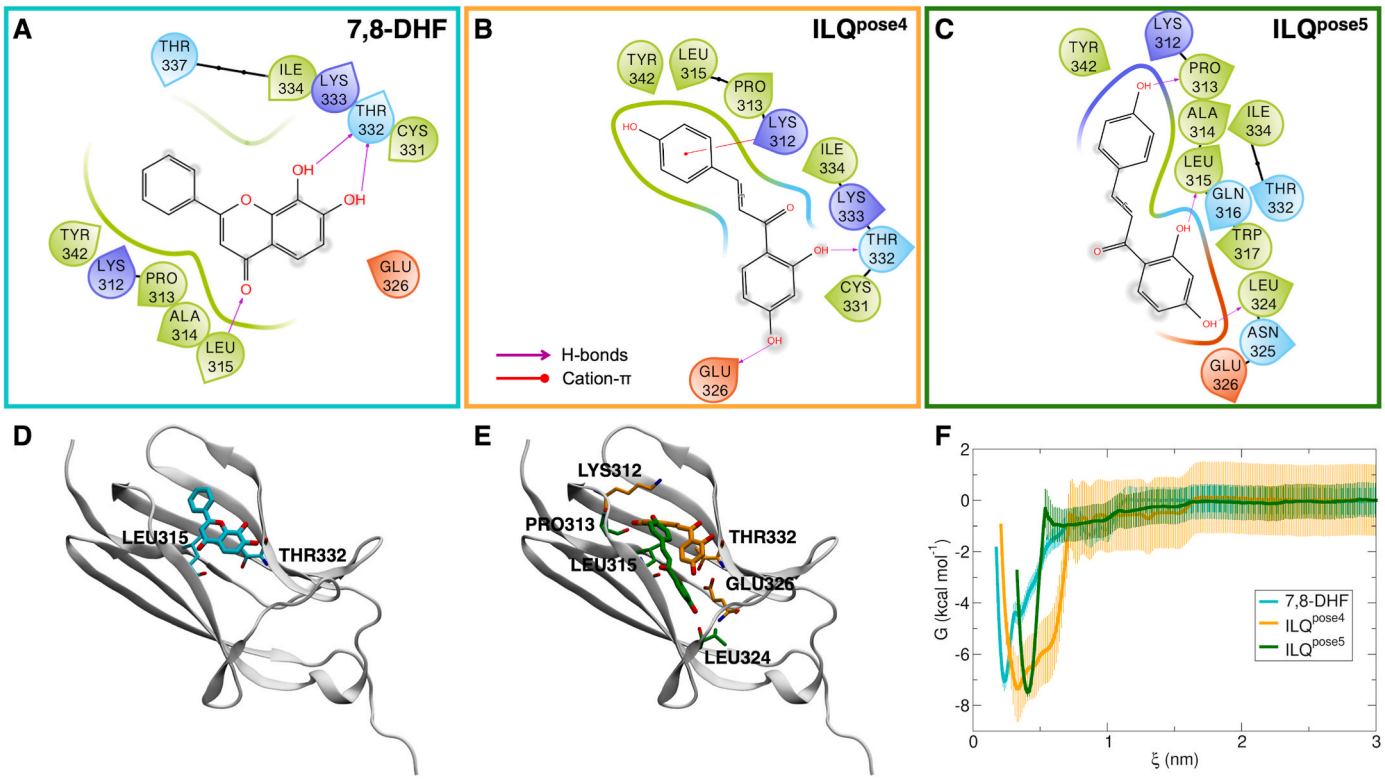

Fig. 5. Interaction diagrams of induced-fit docking poses for 7,8-DHF (A), ILQ^{pose4} (B) and ILQ^{pose5} (C). Structure of induced-fit docking poses for 7,8-DHF (D), ILQ^{pose4} and ILQ^{pose5} (E) in complex with TrkB, where the C atoms of the ligand and the interacting residues are colored according to the legend in panel (F), O atoms are shown in red and N atoms in blue. Free energy profile for 7,8-DHF, ILQ^{pose4} and ILQ^{pose5} binding to TrkB calculated with the SMD/US method along the reaction coordinate ξ (F). The error range is represented by vertical bars. (For interpretation of the references to color in this figure legend, the reader is referred to the Web version of this article.)

than, that of 7,8-DHF, although the difference is not statistically significant. The other ILQ poses present moderate (ILQ^{pose1}, ILQ^{pose3}, ILQ^{pose8}) or small (ILQ^{pose2}, ILQ^{pose6}, ILQ^{pose7}) Δ $G_{binding}$ values.

In conclusion, by means of a combination of docking and SMD/US calculations, we have found that ILQ can stably bind TrkB by at least two different configurations, as strongly as 7,8-DHF, which has been established as TrkB agonist, mimicking BDNF functions.

3.4. *Influence of temperature on free ILQ stability for in vitro validation*

To confirm evidence from computational studies and to compare the biological activity of the free ILQ and the nano-ILQ, in vitro evaluations were performed using SH-SY5Y cell line stably expressing TrkB receptor. Cell viability was assessed by MTT assays using the selective TrkB antagonist ANA-12 and rotenone to demonstrate the increased cell viability when ILQ and nano-ILQ bind TrkB (3.6.2 paragraph). Prior to the in vitro assays, stability studies by UV-vis spectrophotometry were performed.

The stability of 7,8-DHF and ILQ in solution was monitored at predefined time intervals to calculate the degradation kinetics. As far as we know, kinetics of 7,8-DHF and ILQ degradation in DMSO at 37 °C has not been explored. Thus, the stability evaluation at these conditions was performed via a spectrophotometric study, in view of in vitro studies. The data presented in Fig. 6A showed that 7,8-DHF stability was maintained within 168 h of storage at experimental conditions. The initial concentration of ILQ (ILQ_0) decreased by approximately 10% after 72 h of storage and decreased by 25% after 168 h of storage at 37 °C (Fig. 6B).

Kinetic models can be used to predict the decay process of drugs under certain conditions.

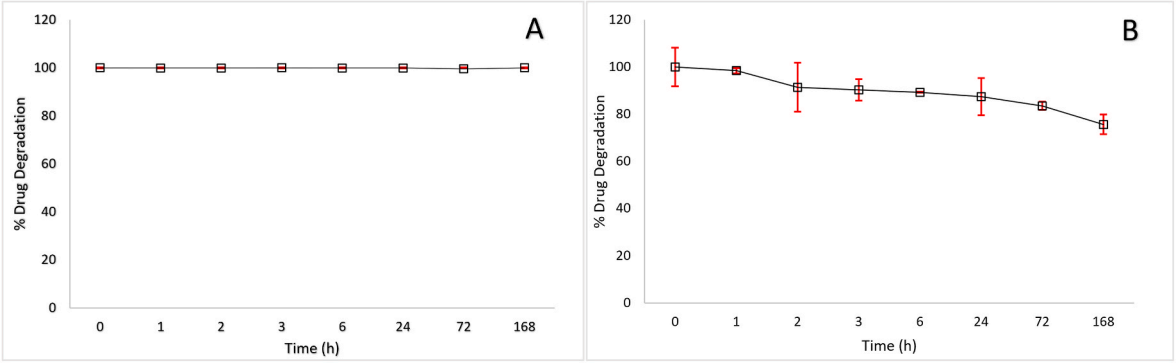

Fig. 6. In solution stability analysis. Degradation profiles of 7,8-DHF (A) and ILQ (B) incubated in vitro at 37 °C in DMSO (20 μg/mL).

A kinetics study was evaluated by using the zero, first, and second order kinetic models of the linear type. The relevant formulas are shown in the following equation.

Zero-order kinetics is expressed as:

$$C_t = -k_0 t + C_0$$

First-order kinetics is expressed as:

$$ln\ C_t = -k_1 t + \ln C_0$$

Second-order kinetics is expressed as:

$$C_t = \frac{1}{\frac{1}{C_0} + k_2 t}$$

Where C_0 and C_t are the initial concentration and concentration after time t; k0, k1, and k2 are the rate constants of zero-order, first-order, and second-order equations, respectively. Graphs of C_t versus t, ln C_t versus t, and $1/C_t$ versus t were plotted to check whether the degradation of ILQ obeys first, second, or zero-order kinetics (Fig. 7).The data obtained from the previous experiments using zero, first-, and second-order equations are tabulated in Table 5, along with the rate constants and correlation coefficient (R^2) values [50] C_t (at T_0) versus t (168 h) was selected for ILQ (Table 5).

As reported in Table 5, the best linear correlation was obtained with the second-order model (R^2 = 0.8258), compared to the first-order (R^2 = 0.7884) and zero-order (R^2 = 0.7479) fits. Although the calculated initial concentrations (C_0 = 15.15 μg/ml for first-order and C_0 = 15.13 μg/ml for second-order) slightly underestimated the experimental value (C_0 = 20 μg/ml), the second-order model provided the best overall fit and the most consistent description of the degradation process. The second-order rate constant ($k_2 = 9.58 \times 10^{-5}$ mL) indicates a slow degradation process, suggesting that ILQ is relatively stable under physiological temperature.

3.4.1. *In vitro effects against rotenone toxicity in neuronal-like SH-SY5Y cells*

Prior to conducting in vitro studies, the pH and osmolality of both the starter formulation (7.8 mM) and the formulation used for in vitro studies (at a final concentration of 10 μM) were also evaluated. The pH values of the undiluted and diluted formulations were 6.7 and 7.4, respectively. Regarding osmolality, the undiluted formulation was found to be hypertonic (~1973 mOsm/kg), while dilution resulted in a hypotonic solution (~117 mOsm/kg). However, once the diluted formulation was mixed with the cell culture medium, the final preparation achieved isotonicity, making it suitable for cell-based assays without risk of osmotic stress.

Nanonization process could affect biological activity influencing dissolution rate of ILQ, for this purpose ILQ and nano-ILQ were tested for their ability to protect neuronal-like SH-SY5Y cells from rotenone toxicity through TrkB activation. This model was chosen as it is well established to study neurotoxicity in this cell line, using the MTT viability assay [51–53]. In particular, a concentration of rotenone suitable for protection studies was selected based on our previously published work on the same cell line [51]. The TrkB receptor agonist 7, 8-DHF was used as a positive control to confirm neuroprotection by receptor activation. As reported in Fig. 8, treatment with rotenone (ROT; 150 nM) for 24 h significantly reduced SH-SY5Y cell viability, an effect prevented by the addition of ILQ, nano-ILQ or 7,8-DHF (all at 10 μM) starting 30 min prior to the toxic stimulus. The pharmacological inhibition of the TrkB receptor with the selective antagonist ANA-12 was then carried out to prove its involvement in the observed effects. As shown in Fig. 8, pre-treatment for 30 min with ANA12 (10 μM) was able to prevent the neuroprotective effects of all three drugs. Such results are in agreement with previous studies reporting that activation of the TrkB receptor is neuroprotective against rotenone-mediated neurotoxicity, both in vivo and in vitro [54,55].

4. Conclusions

This study demonstrates that DoE approach is a good statistical and predictive tool to obtain an optimized formulation by reducing the number of experiments and raw material consumption. Furthermore, highlighting the influence of independent variables (concentration and stabilizer type) on dependent variables (mean size and Zeta potential), it was possible to obtain an optimized formulation with a uniform mean size (81.87 ± 0.5 nm) and a highly negative Zeta potential (−38.36 ± 0.46 mV). Long-term stability studies revealed promising results showing a stable formulation (stored at 4 °C) for six months. The pH and osmolarity values confirm the compatibility of the optimized formulation with in vitro applications.

MD simulations provided evidence that ILQ possesses a binding affinity to the TrkB receptor comparable to the agonist 7,8-DHF. Docking and Umbrella Sampling calculations revealed the stability of the ILQ-TrkB interaction in two binding poses, with free energy values similar to those observed for 7,8-DHF, supporting a favorable and persistent interaction with the receptor.

These computational findings were validated by in vitro studies performed in SH-SY5Y neuronal cells. Both ILQ and, more significantly, nano-ILQ attenuated rotenone-induced toxicity on pre-treated cells with selective TrkB antagonist ANA-12, confirming direct involvement of the receptor. Compared to free ILQ, nano-ILQ exhibited superior biological activity, probably due to their enhanced solubility and bioavailability resulting from nanonized formulation. Overall, the present data supports the potential role of nano-ILQ as promising candidates for the development of small-molecule TrkB agonists, potentially offering a novel therapeutic strategy for neurodegenerative diseases in which BDNF-TrkB signaling is impaired. Beyond its neuroprotective potential, the rational combination of nanocrystal technology with natural bioactive compounds such as ILQ is a good approach for enhancing the translational applications. Future work should focus on improving the long-term stability of nano-ILQ, investigating their pharmacokinetic and biodistribution profiles in animal models, and evaluating the TrkB activation in vivo.

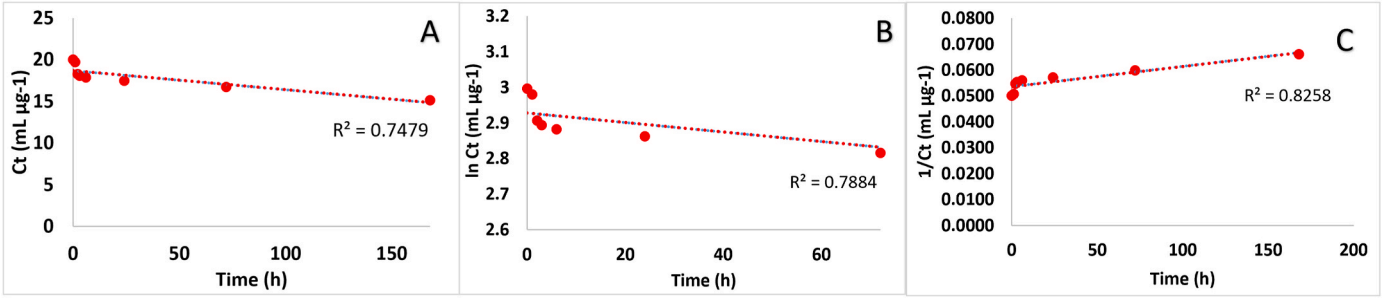

Fig. 7. Zero order (A), first order (B), second order (C) kinetic plots of ILQ.

Table 5
Kinetic parameters ILQ degradation[a].

Drug	Zero-order			First-order			Second-order		
ILQ	$C_{0\ (cal.)}$ (μg mL^{-1})	R^2	K_0 (μg $^{-1}$ h^{-1})	$C_{0\ (cal.)}$ (μg mL^{-1})	R^2	K_1 (μg $^{-1}$ h^{-1})	$C_{0\ (cal.)}$ (μg mL^{-1})	R^2	K_2 (μg $^{-1}$ h^{-1})
	24.87	0.7479	0.029	15.15	0.7884	0.00165	15.13	0.8258	9.58×10^{-5}

[a] Initial ILQ concentration (C_0) = 20 μg/mL.

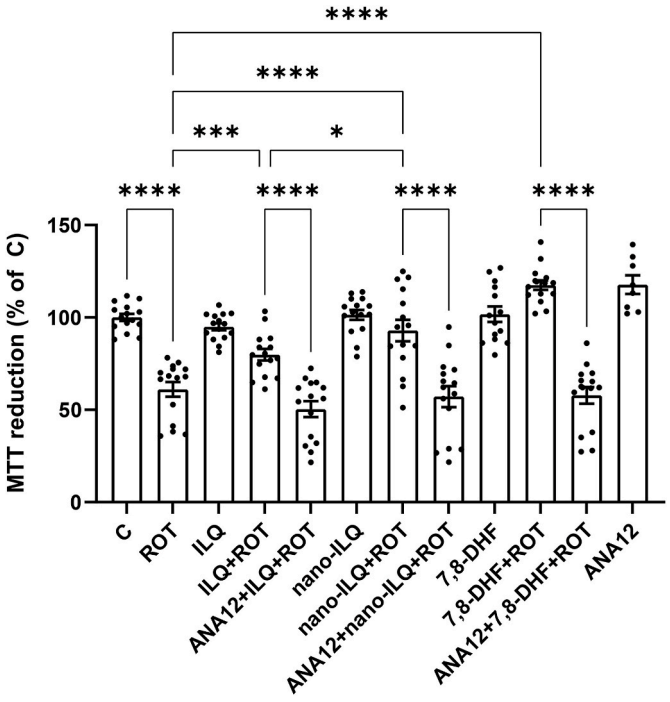

Fig. 8. MTT viability assay on SH-SY5Y cells challenged with rotenone (ROT; 150 nM) alone and in the presence of ILQ, nano-ILQ or 7,8-DHF (each 10 μM) with or without the Trk-B receptor antagonist ANA12 (10 μM). Bars are the means ± SEM of at least 3 independent experiments. *$p < 0.05$ and ****$p < 0.0001$ by one way ANOVA followed by Fisher's LSD post-hoc test.

Consent for publication

All authors have read and approved the manuscript and it has not been published elsewhere, nor is it currently under consideration for publication elsewhere.

Funding

This study belongs to the project HEAL Italia - Health Extended Alliance for Innovative Therapies, Advanced Lab-research, and Integrated Approaches of Precision Medicine, funded by PNRR-NextGenerationEU (Missione 4, Componente 2 "Dalla ricerca all'impresa") to Rosario Pignatello CUP E63C22002080006 of the University of Catania. The views and opinions expressed are those of the authors only, and do not necessarily reflect those of the European Union or the European Commission. Neither the European Union nor European Commission can be held responsible for them.

S. Manin is recipient of a PhD grantship in Basic and Applied Biomedical Sciences, cycle XXXIX, within this project. S.S. has been supported by the International Ph.D. program in Neuroscience, University of Catania. The research leading to these results has received funding from the European Union – NextGenerationEU through the Italian Ministry of University and Research under PNRR.

The research leading to these results has received funding from the European Union – NextGenerationEU through the Italian Ministry of University and Research under PNRR – M4C2-I1.3 Project PE_00000019 "HEAL ITALIA" to Prof. Cristiana Di Valentin CUP H43C22000830006 of the University of Milano-Bicocca.

CRediT authorship contribution statement

Sara Manin: Data curation, Investigation, Methodology, Writing – original draft. **Edoardo Donadoni:** Data curation, Investigation, Methodology, Writing – original draft. **Sara Merlo:** Data curation, Investigation, Methodology, Writing – original draft. **Angela Bonaccorso:** Data curation, Writing – original draft. **Sonya Salamone:** Investigation, Methodology, Writing – original draft. **Giulia Frigerio:** Investigation, Methodology, Writing – original draft. **Paulo Siani:** Investigation, Methodology, Writing – original draft. **Josè Maria Lo Faro:** Investigation, Methodology, Writing – original draft. **Teresa Musumeci:** Conceptualization, Formal analysis, Project administration, Writing – review & editing. **Cristiana Di Valentin:** Conceptualization, Formal analysis, Project administration, Writing – review & editing. **Rosario Pignatello:** Conceptualization, Formal analysis, Project administration, Writing – review & editing.

Declaration of competing interest

The authors declare that they have no known competing financial interests or personal relationships that could have appeared to influence the work reported in this paper.

Acknowledgments

A.B. is a Researcher at the University of Catania within the EU funded PON REACT project (Azione IV.4 – 'Dottorati e contratti di ricerca su tematiche dell'innovazione', nuovo Asse IV del PON Ricerca e Innovazione 2014–2020 'Istruzione e ricerca per il recupero– REACT – EU'; Progetto 'Approcci terapeutici innovativi per il targeting cerebrale di farmaci e materiale genico', CUP E65F21002640005).

Appendix A. Supplementary data

Supplementary data to this article can be found online at https://doi.org/10.1016/j.jddst.2026.108520.

Data availability

The data sets generated during and/or analyzed during the current study are available from the corresponding author on reasonable request.

References

[1] N. Nasim, I.S. Sandeep, S. Mohanty, Plant-derived natural products for drug discovery: current approaches and prospects, The Nucleus: Int. J. Cytol. Allied Topics 65 (3) (2022) 399–411, https://doi.org/10.1007/s13237-022-00405-3.
[2] J.-Y. Kim, S.J. Park, K.-J. Yun, Y.-W. Cho, H.-J. Park, K.-T. Lee, Isoliquiritigenin isolated from the roots of Glycyrrhiza uralensis inhibits LPS-induced iNOS and COX-2 expression via the attenuation of NF-kappaB in RAW 264.7 macrophages, Eur. J. Pharmacol. 584 (1) (2008) 175–184, https://doi.org/10.1016/j.ejphar.2008.01.032.
[3] F. Peng, Q. Du, C. Peng, N. Wang, H. Tang, X. Xie, J. Shen, J. Chen, A review: the pharmacology of isoliquiritigenin, Phytother Res.: PTR 29 (7) (2015) 969–977, https://doi.org/10.1002/ptr.5348.

[4] D. Shi, J. Yang, Y. Jiang, L. Wen, Z. Wang, B. Yang, The antioxidant activity and neuroprotective mechanism of isoliquiritigenin, Free Radic. Biol. Med. 152 (2020) 207–215, https://doi.org/10.1016/j.freeradbiomed.2020.03.016.
[5] K.-L. Wang, Y.-C. Yu, S.-M. Hsia, Perspectives on the role of isoliquiritigenin in cancer, Cancers 13 (1) (2021) 115, https://doi.org/10.3390/cancers13010115.
[6] L. Zhao, M. Li, Q. Zhu, H. Yang, Y. Zhao, Anti-obesity effect of isoliquiritigenin in the 3T3-L1 cell line and a high-fat diet-induced obesity mice model, J. Funct.Foods 127 (2025) 106735, https://doi.org/10.1016/j.jff.2025.106735.
[7] X. Zhu, J. Liu, S. Huang, W. Zhu, Y. Wang, O. Chen, J. Xue, Neuroprotective effects of isoliquiritigenin against cognitive impairment *via* suppression of synaptic dysfunction, neuronal injury, and neuroinflammation in rats with kainic acid-induced seizures, Int. Immunopharmacol. 72 (2019) 358–366, https://doi.org/10.1016/j.intimp.2019.04.028.
[8] M.R. Gigliobianco, C. Casadidio, R. Censi, P. Di Martino, Nanocrystals of poorly soluble drugs: drug bioavailability and physicochemical stability, Pharmaceutics 10 (3) (2018) 134, https://doi.org/10.3390/pharmaceutics10030134.
[9] Y. Ma, X. Yang, G. Chen, H. Zhang, Y. Zhang, W. Zhang, Effect of particle size on the oral absorption of isoliquiritigenin nanocrystals, Brazilian J. Pharmac. Sci. 58 (2022), https://doi.org/10.1590/s2175-97902022e201186.
[10] E. Zingale, A. Bonaccorso, C. Carbone, T. Musumeci, R. Pignatello, Drug nanocrystals: focus on brain delivery from therapeutic to diagnostic applications, Pharmaceutics 14 (4) (2022) 691, https://doi.org/10.3390/pharmaceutics14040691.
[11] L. Gao, G. Liu, J. Ma, X. Wang, L. Zhou, X. Li, F. Wang, Application of drug nanocrystal technologies on oral drug delivery of poorly soluble drugs, Pharm. Res. 30 (2) (2013) 307–324, https://doi.org/10.1007/s11095-012-0889-z.
[12] A. Tuomela, J. Hirvonen, L. Peltonen, Stabilizing agents for drug nanocrystals: effect on bioavailability, Pharmaceutics 8 (2) (2016) 16, https://doi.org/10.3390/pharmaceutics8020016.
[13] H. Yang, H. Kim, S. Jung, H. Seo, S.K. Nida, S.-Y. Yoo, J. Lee, Pharmaceutical strategies for stabilizing drug nanocrystals, Curr. Pharm. Des. 24 (21) (2018) 2362–2374, https://doi.org/10.2174/1381612824666180515125247.
[14] D. Gol, S. Thakkar, M. Misra, Nanocrystal-based drug delivery system of risperidone: lyophilization and characterization, Drug Dev. Ind. Pharm. 44 (9) (2018) 1458–1466, https://doi.org/10.1080/03639045.2018.1460377.
[15] T. Liu, X. Yu, H. Yin, J.P. Möschwitzer, Advanced modification of drug nanocrystals by using novel fabrication and downstream approaches for tailor-made drug delivery, Drug Deliv. 26 (1) (2019) 1092–1103, https://doi.org/10.1080/10717544.2019.1682721.
[16] A. Bonaccorso, M.R. Gigliobianco, R. Pellitteri, D. Santonocito, C. Carbone, P. Di Martino, G. Puglisi, T. Musumeci, Optimization of Curcumin nanocrystals as promising strategy for nose-to-brain delivery application, Pharmaceutics 12 (5) (2020) 476, https://doi.org/10.3390/pharmaceutics12050476.
[17] A. Bonaccorso, M.R. Gigliobianco, R. Lombardo, R. Pellitteri, P. Di Martino, A. Mancuso, T. Musumeci, Nanonized carbamazepine for nose-to-brain delivery: pharmaceutical formulation development, Pharmaceut. Dev. Technol. 28 (2) (2023) 248–263, https://doi.org/10.1080/10837450.2023.2177673.
[18] L. de O. Macedo, E.J. Barbosa, R. Löbenberg, N.A. Bou-Chacra, Anti-inflammatory drug nanocrystals: state of art and regulatory perspective, Eur. J. Pharmaceut. Sci.: Off. J. Eur. Feder. Pharmac. Sci. 158 (2021) 105654, https://doi.org/10.1016/j.ejps.2020.105654.
[19] X. Zhu, J. Liu, S. Chen, J. Xue, S. Huang, Y. Wang, O. Chen, Isoliquiritigenin attenuates lipopolysaccharide-induced cognitive impairment through antioxidant and anti-inflammatory activity, BMC Neurosci. 20 (1) (2019) 41, https://doi.org/10.1186/s12868-019-0520-x.
[20] T.A. Gudasheva, A.V. Tallerova, A.G. Mezhlumyan, T.A. Antipova, I.O. Logvinov, Y.N. Firsova, P.Y. Povarnina, S.B. Seredenin, Low-molecular weight BDNF mimetic, dimeric dipeptide GSB-106, reverses depressive symptoms in mouse chronic social defeat stress, Biomolecules 11 (2) (2021) 252, https://doi.org/10.3390/biom11020252.
[21] S.-W. Jang, X. Liu, M. Yepes, K.R. Shepherd, G.W. Miller, Y. Liu, W.D. Wilson, G. Xiao, B. Blanchi, Y.E. Sun, K. Ye, A selective TrkB agonist with potent neurotrophic activities by 7,8-dihydroxyflavone, Proc. Natl. Acad. Sci. U. S. A 107 (6) (2010) 2687–2692, https://doi.org/10.1073/pnas.0913572107.
[22] Z. Zhang, X. Liu, J.P. Schroeder, C.-B. Chan, M. Song, S.P. Yu, D. Weinshenker, K. Ye, 7,8-dihydroxyflavone prevents synaptic loss and memory deficits in a mouse model of Alzheimer's disease, Neuropsychopharmacology: Off. Publ. Am. College Neuropsychopharmacol. 39 (3) (2014) 638–650, https://doi.org/10.1038/npp.2013.243.
[23] G. Schirò, S. Iacono, P. Ragonese, P. Aridon, G. Salemi, C.R. Balistreri, A brief overview on BDNF-Trk pathway in the nervous system: a potential biomarker or possible target in treatment of multiple sclerosis? Front. Neurol. 13 (2022) https://doi.org/10.3389/fneur.2022.917527.
[24] M.J. Banfield, R.L. Naylor, A.G.S. Robertson, S.J. Allen, D. Dawbarn, R.L. Brady, Specificity in trk receptor:neurotrophin interactions: the crystal structure of TrkB-d5 in complex with Neurotrophin-4/5, Structure 9 (12) (2001) 1191–1199, https://doi.org/10.1016/S0969-2126(01)00681-5.
[25] G.M. Sastry, M. Adzhigirey, T. Day, R. Annabhimoju, W. Sherman, Protein and ligand preparation: parameters, protocols, and influence on virtual screening enrichments, J. Comput. Aided Mol. Des. 27 (3) (2013) 221–234, https://doi.org/10.1007/s10822-013-9644-8.
[26] T.A. Halgren, R.B. Murphy, R.A. Friesner, H.S. Beard, L.L. Frye, W.T. Pollard, J. L. Banks, Glide: a new approach for rapid, accurate docking and scoring. 2. Enrichment factors in database screening, J. Med. Chem. 47 (7) (2004) 1750–1759, https://doi.org/10.1021/jm030644s.
[27] J.L. Banks, H.S. Beard, Y. Cao, A.E. Cho, W. Damm, R. Farid, A.K. Felts, T. A. Halgren, D.T. Mainz, J.R. Maple, R. Murphy, D.M. Philipp, M.P. Repasky, L. Y. Zhang, B.J. Berne, R.A. Friesner, E. Gallicchio, R.M. Levy, Integrated modeling program, applied chemical theory (IMPACT), J. Comput. Chem. 26 (16) (2005) 1752–1780, https://doi.org/10.1002/jcc.20292.
[28] S. Jo, T. Kim, V.G. Iyer, W. Im, CHARMM-GUI: a web-based graphical user interface for CHARMM, J. Comput. Chem. 29 (11) (2008) 1859–1865, https://doi.org/10.1002/jcc.20945.
[29] J. Huang, A.D. MacKerell, CHARMM36 all-atom additive protein force field: validation based on comparison to NMR data, J. Comput. Chem. 34 (25) (2013) 2135–2145, https://doi.org/10.1002/jcc.23354.
[30] I. Soteras Gutiérrez, F.-Y. Lin, K. Vanommeslaeghe, J.A. Lemkul, K.A. Armacost, C. L. Brooks, A.D. MacKerell, Parametrization of halogen bonds in the CHARMM general force field: improved treatment of ligand-protein interactions, Bioorg. Med. Chem. 24 (20) (2016) 4812–4825, https://doi.org/10.1016/j.bmc.2016.06.034.
[31] K. Vanommeslaeghe, E. Hatcher, C. Acharya, S. Kundu, S. Zhong, J. Shim, E. Darian, O. Guvench, P. Lopes, I. Vorobyov, A.D. Mackerell, CHARMM general force field: a force field for drug-like molecules compatible with the CHARMM all-atom additive biological force fields, J. Comput. Chem. 31 (4) (2010) 671–690, https://doi.org/10.1002/jcc.21367.
[32] K. Vanommeslaeghe, E.P. Raman, A.D. MacKerell, Automation of the CHARMM general force field (CGenFF) II: assignment of bonded parameters and partial atomic charges, J. Chem. Inf. Model. 52 (12) (2012) 3155–3168, https://doi.org/10.1021/ci3003649.
[33] A.D. MacKerell, D. Bashford, M. Bellott, R.L. Dunbrack, J.D. Evanseck, M.J. Field, S. Fischer, J. Gao, H. Guo, S. Ha, D. Joseph-McCarthy, L. Kuchnir, K. Kuczera, F. T. Lau, C. Mattos, S. Michnick, T. Ngo, D.T. Nguyen, B. Prodhom, M. Karplus, All-atom empirical potential for molecular modeling and dynamics studies of proteins, J. Phys. Chem. B 102 (18) (1998) 3586–3616, https://doi.org/10.1021/jp973084f.
[34] M.J. Abraham, T. Murtola, R. Schulz, S. Páll, J.C. Smith, B. Hess, E. Lindahl, GROMACS: high performance molecular simulations through multi-level parallelism from laptops to supercomputers, SoftwareX 1–2 (2015) 19–25, https://doi.org/10.1016/j.softx.2015.06.001.
[35] D. Beglov, B. Roux, Finite representation of an infinite bulk system: solvent boundary potential for computer simulations, J. Chem. Phys. 100 (12) (1994) 9050–9063, https://doi.org/10.1063/1.466711.
[36] S.Y. Noskov, B. Roux, Control of ion selectivity in LeuT: two Na+ binding sites with two different mechanisms, J. Mol. Biol. 377 (3) (2008) 804–818, https://doi.org/10.1016/j.jmb.2008.01.015.
[37] G. Bussi, D. Donadio, M. Parrinello, Canonical sampling through velocity rescaling, J. Chem. Phys. 126 (1) (2007) 014101, https://doi.org/10.1063/1.2408420.
[38] M. Parrinello, A. Rahman, Polymorphic transitions in single crystals: a new molecular dynamics method, J. Appl. Phys. 52 (12) (1981) 7182–7190, https://doi.org/10.1063/1.328693.
[39] B. Hess, H. Bekker, H.J.C. Berendsen, J.G.E.M. Fraaije, LINCS: a linear constraint solver for molecular simulations, J. Comput. Chem. 18 (12) (1997) 1463–1472, https://doi.org/10.1002/(SICI)1096-987X(199709)18:12<1463::AID-JCC4>3.0.CO;2-H.
[40] T. Darden, D. York, L. Pedersen, Particle mesh Ewald: an N·log(N) method for Ewald sums in large systems, J. Chem. Phys. 98 (12) (1993) 10089–10092, https://doi.org/10.1063/1.464397.
[41] B. Roux, The calculation of the potential of mean force using computer simulations, Comput. Phys. Commun. 91 (1) (1995) 275–282, https://doi.org/10.1016/0010-4655(95)00053-I.
[42] D. Jakubec, J. Vondrášek, Can all-atom molecular dynamics simulations quantitatively describe Homeodomain-DNA binding equilibria? J. Chem. Theor. Comput. 15 (4) (2019) 2635–2648, https://doi.org/10.1021/acs.jctc.8b01144.
[43] M. Danaei, M. Dehghankhold, S. Ataei, F. Hasanzadeh Davarani, R. Javanmard, A. Dokhani, S. Khorasani, M.R. Mozafari, Impact of particle size and polydispersity index on the clinical applications of lipidic nanocarrier systems, Pharmaceutics 10 (2) (2018), https://doi.org/10.3390/pharmaceutics10020057. Articolo 2.
[44] Safo, I. A., Werheid, M., Dosche, C., & Oezaslan, M. (s.d.). The role of polyvinylpyrrolidone (PVP) as a capping and structure-directing agent in the formation of Pt nanocubes. Nanoscale Adv., 1(8), 3095–3106. https://doi.org/10.1039/c9na00186g.
[45] H. Wen, K.R. Morris, K. Park, Study on the interactions between Polyvinylpyrrolidone (PVP) and acetaminophen crystals: partial dissolution pattern change, J. Pharmaceut. Sci. 94 (10) (2005) 2166–2174, https://doi.org/10.1002/jps.20383.
[46] D. Jain, R. Athawale, A. Bajaj, S. Shrikhande, P.N. Goel, R.P. Gude, Studies on stabilization mechanism and stealth effect of poloxamer 188 onto PLGA nanoparticles, Colloids Surf. B Biointerfaces 109 (2013) 59–67, https://doi.org/10.1016/j.colsurfb.2013.03.027.
[47] C.C. Trujillo, A.J. Wright, Properties and stability of solid lipid particle dispersions based on Canola Stearin and Poloxamer 188, JAOCS (J. Am. Oil Chem. Soc.) 87 (7) (2010) 715–730, https://doi.org/10.1007/s11746-010-1553-6.
[48] S.V. Jermain, C. Brough, R.O. Williams, Amorphous solid dispersions and nanocrystal technologies for poorly water-soluble drug delivery – an update, Int. J. Pharm. 535 (1) (2018) 379–392, https://doi.org/10.1016/j.ijpharm.2017.10.051.
[49] N. Chitranshi, V. Gupta, S. Kumar, S.L. Graham, Exploring the molecular interactions of 7,8-Dihydroxyflavone and its derivatives with TrkB and VEGFR2 proteins, Int. J. Mol. Sci. 16 (9) (2015) 9, https://doi.org/10.3390/ijms160921087.
[50] S. Sen, C. Das, N. Nath Ghosh, N. Baildya, S. Bhattacharya, M. Ali Khan, M. Sillanpää, G. Biswas, Is degradation of dyes even possible without using

photocatalysts? – a detailed comparative study, RSC Adv. 12 (53) (2022) 34335–34345, https://doi.org/10.1039/D2RA05779D.
[51] M. Beneventano, S.F. Spampinato, S. Merlo, M. Chisari, P. Platania, M. Ragusa, M. Purrello, F. Nicoletti, M.A. Sortino, Shedding of microvesicles from Microglia contributes to the effects induced by metabotropic glutamate receptor 5 activation on neuronal death, Front. Pharmacol. 8 (2017) 812, https://doi.org/10.3389/fphar.2017.00812.
[52] X. Li, W. Li, X. Xie, T. Fang, J. Yang, Y. Shen, Y. Wang, H. Wang, L. Tao, H. Zhang, ROS regulate rotenone-induced SH-SY5Y dopamine neuron death through ferroptosis-mediated autophagy and apoptosis, Mol. Neurobiol. 62 (7) (2025) 9271–9289, https://doi.org/10.1007/s12035-025-04824-6.
[53] M. Ramkumar, S. Rajasankar, V.V. Gobi, C. Dhanalakshmi, T. Manivasagam, A. Justin Thenmozhi, M.M. Essa, A. Kalandar, R. Chidambaram, Neuroprotective effect of Demethoxycurcumin, a natural derivative of Curcumin on rotenone induced neurotoxicity in SH-SY 5Y Neuroblastoma cells, BMC Compl. Alternative Med. 17 (2017) 217, https://doi.org/10.1186/s12906-017-1720-5.
[54] S. Nie, K. Ma, M. Sun, M. Lee, Y. Tan, G. Chen, Z. Zhang, Z. Zhang, X. Cao, 7,8-Dihydroxyflavone protects nigrostriatal dopaminergic neurons from rotenone-induced neurotoxicity in rodents, Parkinsons Dis. 2019 (2019) 9193534, https://doi.org/10.1155/2019/9193534.
[55] M. Zhu, C. Lu, W. Li, Transient exposure to echinacoside is sufficient to activate Trk signaling and protect neuronal cells from rotenone, J. Neurochem. 124 (4) (2013) 571–580, https://doi.org/10.1111/jnc.12103.